ACS OMEGA

http://pubs.acs.org/journal/acsodf

Article

Transition Metal-Promoted Mg-Fe Mixed Oxides for Conversion of Ethanol to Valuable Products

Jáchym Mück, Jaroslav Kocík,* Karel Frolich, Josef Šimek, Martina Michálková, and Martin Hájek

Cite This: *ACS Omega* 2023, 8, 19374−19384

Read Online

ACCESS | Metrics & More | Article Recommendations | Supporting Information

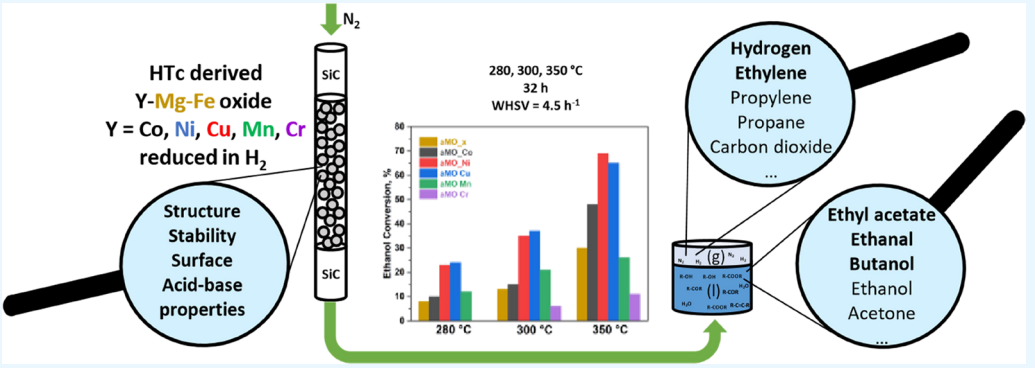

ABSTRACT: The conversion of ethanol into petrochemicals, such as ethyl and butyl acetate, butanol, hexanol, and so forth was studied. The conversion was catalyzed by Mg-Fe mixed oxide modified with a second transition metal (Ni, Cu, Co, Mn, or Cr). The main aim was to describe the influence of second transition metal on (i) the catalyst itself and (ii) reaction products such as ethyl acetate, butanol, hexanol, acetone, and ethanal. Moreover, the results were compared with the results of pure Mg-Fe. The reaction was carried out in the gas phase in a flow reactor with a weight hour space velocity of 4.5 h^{-1} for 32 h at three reaction temperatures (280, 300, and 350 °C). The metals Ni and Cu in Mg-Fe oxide enhanced the ethanol conversion due to the population of active dehydrogenation sites. Despite the lower acido-basicity, Cu, Co, and Ni supported the yield of ethyl acetate, and Cu and Ni also promoted the yield of higher alcohols. Ni was related to the extent of the gasification reactions. Moreover, long-term stability (by leaching of metals) test was carried out for all catalysts (128 h).

1. INTRODUCTION

Increasing awareness of environmental pollution and the limited amount of fossil resources have increased the effort for using renewable "green" raw materials for chemical industry such as vegetable oil, waste cooking oils, and lignocellulose biomass. The sugar base or lignocellulose biomass is used for ethanol production by fermentation. Ethanol has many practical applications in the (petro)chemical industry such as (i) solvent, (ii) additive to gasoline, and (iii) renewable raw material for production of other chemicals, ethanal,[1] esters, ethylene,[2] higher alcohols, higher hydrocarbons, and more, which are usually produced from crude oil.[3,4]

Esters represent a solvent for paint, organic compounds in the food and beverage industry, and also a substitute of aromatic compounds in many applications.[5] For example, toluene can be replaced by ethyl acetate, which is less toxic and environmentally more friendly. Ethyl acetate is mainly produced by three ways: (i) esterification of acetic acid with ethanol, (ii) catalytic addition of acetic acid to ethylene and (iii) Tishchenko reaction.[6] Tishchenko reaction is the disproportionation of two same or different aldehydes to form corresponding esters. The advantage of the Tishchenko reaction is that it is not a corrosive process, but the disadvantage is that the raw materials (aldehydes) are toxic.[7] This problem can be solved when the process of dehydrogenative dimerization of alcohols is used, where the first step is dehydrogenation of alcohol to aldehyde and it is followed by the Tishchenko reaction. Because the aldehydes are very reactive intermediates, they can react not only by the desired reaction pathway but can react to many other reaction ways such as the Guerbet reaction, which produces higher alcohols. The byproducts of the reaction such as butanol, hexanol, hydrogen, and more also have commercial potential because they can be used as fuels, solvents, or raw materials.

The transformation of ethanol is usually heterogeneously catalyzed with oxides, zeolites, and hydroxyapatites at temper-

Received: January 10, 2023
Accepted: May 12, 2023
Published: May 24, 2023

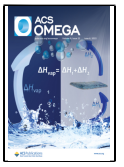

atures around 350 °C,[4,8,9] but a lower temperature is required due to cost and environmental benefits. In general, active catalysts in the conversion of ethanol are bifunctional with disposal of redox and acid−base properties. The distribution of the active sites (metal and acid−base) and mainly the amount of strong basic sites on the surface of a catalyst have an effect on the reaction product composition. In this case, it will be advantageous to use heterogeneous catalysts based on mixed oxides (MOs), which can dispose of these properties depending on their chemical composition. Hydrotalcite-like compounds (hydrotalcite, HT) are usually used as a precursor for the synthesis of MO. With heat treatment, the corresponding MOs are formed. Generally, the Mg-Al MOs are studied, however Mg-Fe MOs have transition metal (TM) in the structure which can lead to a higher amount of active redox sites, and they have higher mechanical strength.

This paper focuses on the influence of various second TMs (Co, Ni, Cu, Mn, or Cr) added during coprecipitation of HT with Mg-Fe MO. The MO were applied as heterogenous catalysts for the transformation of ethanol at three different temperatures in a flow reactor. In-depth experimental characterization of the catalysts was used to determine the main conditions that affect the catalyst activity. The relationship between the acid−base, redox, and structure properties and the activity of the catalysts, in particular, the yield to the products such as ethyl acetate, butanol, hexanol, acetone, and ethanal, has been described. The temperature strongly influenced the ethanol conversion and the yield to considered products.

2. MATERIALS AND METHODS

2.1. Catalyst Preparation. The HT catalyst precursors were synthesized by the coprecipitation method, which was carried out in a stirred glass precipitation reactor (5 dm^3 Syrris Globe, England) at 60 °C and pH (9.5). The cation solution was prepared by dissolving the appropriate metal nitrates in distilled water (total metal concentration was 1 mol dm^{-3}) with the respective molar ratio of metals (Co, Ni, Cu, Mn, or Cr)-Mg-Fe 0.5-2-1. The value of pH at 9.5 was maintained by a solution of KOH (2 mol dm^{-3}) and K_2CO_3 (0.2 mol dm^{-3}), and the cation solution was added (30 mL min^{-1}). The formed precipitate was aged for 1 h, filtered, washed by deionized water (to pH 7), and dried at 60 °C overnight. The MOs were obtained by calcination of dry HT at 500 °C for 3 h, with a temperature ramp of 100 °C h^{-1}.

In the following text, the materials are denoted according to (i) the type of material (hydrotalcite, HT, mixed oxide, MO, and reduced mixed oxide, aMO) and (ii) the third metal in the Mg-Fe structure (x — without, Co, Ni, Cu, Mn, and Cr); for example, MO_Cu is Cu-Mg-Fe mixed oxide and aMO_x is Mg-Fe reduced mixed oxide.

2.2. Testing of Catalysts in Reaction. The catalytic tests of Mg-Fe catalysts were realized in a microflow reactor (Vinci Technologies, France) with reaction conditions set on the basis of literature and our previously paper focusing on Mg-Al MOs.[10] Pure ethanol was purchased from Penta, a.s, with a minimum content of 99.8%.

2 g of Mg-Fe MO in the shaped form (0.224−0.560 mm) was inserted into the reactor, and free spaces under and over the catalyst was filled with inert silicon carbide. The MOs with different TMs have different bulk densities and so have to be mixed with silicon carbide to keep a constant contact time for each MO. The material was in situ (i) calcinated at 500 °C (temperature ramp was 100 °C/h) in a flow of nitrogen (8 L/h) for 3 h and then (ii) activated by reduction at 450 °C in a flow of hydrogen (10 L/h) for 5 h. After activation, the temperature was decreased to 300 °C (50 °C/h) in the flow of nitrogen (8 L/h), and the pressure was increased to 10 Mpa. Ethanol was fed into the reactor (9 g h^{-1}) by a pump in the liquid phase, and the reaction was carried out in the gas phase (the constant weight hourly space velocity was 4.5 h^{-1}). The reaction was conducted at the temperatures of 300, 280, and 350 °C (change 10 °C/h). At each temperature, the catalyst was tested for 32 h, and the liquid and gas phases were analyzed for 4 h each. The reaction was measured at the temperature of 300 °C two times, at the beginning and at the end of the experiments, to study the potential catalyst deactivation during the reaction, that is, the ethanol conversion was determined at the beginning and end at the same reaction conditions.

2.3. Analytical Method. *2.3.1. Inductively Coupled Plasma-Optical Emission Spectrometry.* The real molar ratio of metals (X-Mg-Fe) and the residuum of potassium from the base solution in synthesis materials were determined by inductively coupled plasma-optical emission spectrometry [ICP-OES, Agilent 725 (USA) with optical detection]. Before the analysis, the sample (1 g) was mineralized by p-toluenesulfonic acid (0.1 g) at 500 °C. Subsequently, the sample was dissolved in sulfonic acid (p.a.) and diluted by demineralized water. The metal amount was determined by using the calibration curve method.

2.3.2. Powder X-ray Diffraction. The structure of prepared materials (HT, MO, and aMO) were characterized by powder X-ray diffraction (XRD). A D8 Advance ECO (Bruker, USA) diffractometer applying CuKα radiation (λ = 1.5418 Å) with scanned 2θ interval from 5 to 70° at the rate of 0.04°/s was used. Eva software with the Powder Diffraction File database was used (PDF 2 + 2012, International Centre for Diffraction Data).

2.3.3. Thermogravimetric Analysis. The temperature stability of HT was studied on a thermal gravimetric analyzer (TA instruments Discovery, USA) equipped with a mass spectrometer. The analysis was carried out at the temperature range of 30−900 °C with the temperature ramp 10 °C min^{-1} (flow of nitrogen).

2.3.4. Nitrogen Physisorption. The adsorption/desorption isotherms were determined for aMO (Micromeritics ASAP 2020, USA) at liquid nitrogen temperature (77 K). The specific surface area (S_{BET}) was calculated by the Brunauer, Emmett and Teller (BET) theory. The pore size distribution was calculated by nonlocal density functional theory (NLDFT)-silica equilibrium transition kernel base on the cylindrical pore model.

2.3.5. Temperature-Programmed Reduction. The reducibility of X-Mg-Fe MO was studied with a thermal conductivity detector (Micromeritics AutoChem II 2920, Micromeritics Corp., USA). Temperature-programmed reduction (TPR-H_2) experiment was carried out with the flow of hydrogen gas (10 vol % H_2 in Ar) with the linear temperature ramp of 10 °C min^{-1}. 100 mg of the MO was placed into a U-shaped quartz reactor and thermal pretreated at 500 °C for 1 h in helium flow (25 mL min^{-1}) for elimination of adsorbed gas molecules.

2.3.6. Temperature-Programmed Desorption of NH_3 and CO_2. The acid−base properties of X-Mg-Fe aMO were measured by temperature-programmed desorption (TPD) of NH_3 and CO_2 with a Micromeritics AutoChem II 2920

https://doi.org/10.1021/acsomega.3c00182
ACS Omega 2023, 8, 19374−19384

(Micromeritics Corp., USA) instrument equipped with a mass detector (Pfeiffer Vacuum OmniStar TM GSD 320, USA). TPD experiments were carried out with the flow of helium (25 mL min^{-1}) and the linear temperature ramp of 10 °C min^{-1}. 100 mg of the aMO was placed in a quartz reactor and pretreated with the flow of reducing gas (5 vol % H_2 in Ar, 25 mL min^{-1}) at 450 °C for 1 h.

2.3.7. Determination of Reaction Products. The liquid phase of the reaction mixture was analyzed by gas chromatography with a flame ionization detector (Shimadzu GC-2010, Japan) with a Zebron 624plus (30 m × 0.30 mm × 1.4 μm) column. The method of calibration curve was used. The values of ethanol conversion (X_E) and yield (Y_P) to products (P) were calculated (eqs 1 and 2).

$$X_E = \frac{n_{E0} - n_E}{n_{E0}} \quad (1)$$

$$Y_P = \frac{n_P}{n_{E0}} \cdot \frac{|\nu_E|}{|\nu_P|} \quad (2)$$

where n_{E0} is the amount of ethanol (in moles) added to the reaction and n_E and n_P are determined amounts of ethanol or other products formed by the reaction (in moles). The values ν_E and ν_P are the stochiometric coefficients of ethanol or other products. The content of metals was analyzed by ICP-OES (Agilent 5800 ICP-OES) in the liquid phase.

The gas products were also analyzed. A GC-Agilent 7890 A chromatograph equipped with six columns and two thermal conductivity detectors (determination of permanent gases and hydrogen) and one flame ionization detector (determination of hydrocarbons) was used.

3. RESULTS AND DISCUSSION

3.1. Characterization of Synthesized Materials. The proposed molar ratio of TM/Mg/Fe was 0.5:2:1, and only negligible differences between the determined and proposed were observed (2−4 rel %). The real molar ratios for all MOs are in Table S1.

3.1.1. Powder XRD. The structure of the synthesis materials (HT, MO, and aMO) was determined by XRD (Figure 1).

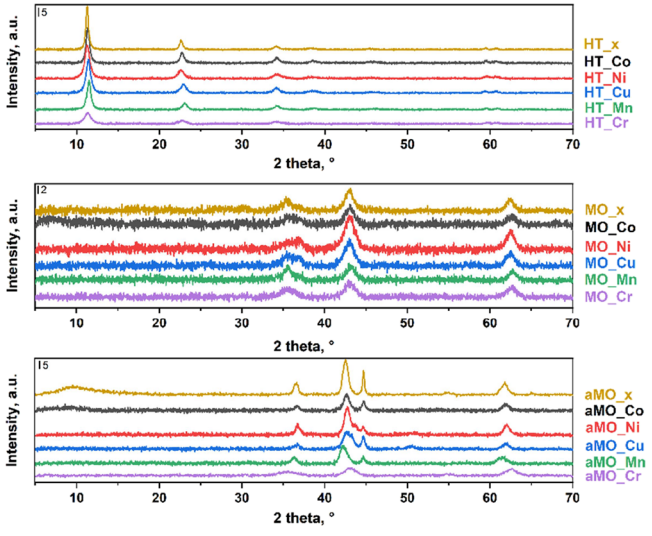

Figure 1. Diffractograms of the synthesized Mg-Fe materials: HT, MOs, and aMOs.

The characteristic sharp diffraction lines with a high intensity of HT are depicted, which demonstrates a well-ordered rhombohedral structure of the prepared HT. The exception is HT with Cr, where the diffraction lines are broader and the crystallographic structure is less defined. The diffraction lines of any other compounds were not observed indicating the presence of the pure HT crystal phase.

The lattice parameters a and c were calculated from diffraction lines at 11 and 59.5° corresponding to (003) and (110) crystal planes, respectively. The lattice parameter a ($a = 2d_{110}$) is described as the distance between the two metal atoms in the crystal lattice. The structure of pyroaurite is derived from brucite (a = 0.3142 nm) with a fraction of Mg substituted by Fe ions. Iron ions has lower ion diameter (64 pm) than Mg (72 pm),[11] and therefore the lattice parameter a is lower for pyroaurite than for brucite. The lattice parameter a for HT_x was determined at 0.3106 nm, which is slightly lower than that published by K.B. Rozov et al. (0.3111 nm).[12] The incorporation of the second TM to the HT structure leads to the change of the lattice parameter a (Table 1). The value of the parameter a is in positive correlation with the diameter of the TM ion. Although the diameter of the Mn^{2+} ion is 83 pm, the lattice parameter a for aMO_Mn is slightly lower than for pure HT_x (pyroaurite), which is probably due to the partial amount of Mn built into the HT structure as trivalent ions (64.5 pm).[13] On the other hand, no correlations were observed for the lattice parameter c (describing the distance of three layers, determined as $c = 3d_{003}$). The parameter c depended on the amount and type of bonded anions and water and the distance of the metal in the crystal lattice which were the same for all prepared HTs.[14]

Table 1. Parameters of Synthesized Mg-Fe HT Calculated from XRD

type of TM	ion diameter, pm	a, nm	c, nm	D, nm
x		0.3106	2.3565	19.0
Co^{+II}	74.5	0.3106	2.3430	15.8
Ni^{+II}	69.0	0.3097	2.3544	12.4
Cu^{+II}	87.0	0.3108	2.3269	13.4
Mn^{+II}/Mn^{+III}	83.0/64.5	0.3104	2.3138	15.3
Cr^{+III}	61.5	0.3099	2.3436	9.3

The crystal size (D) of HT was calculated by the Scherer equation from (003) crystal planes and ranged from 9.3 to 19 nm (Table 1). The built of TM in the structure leads to decrease of the crystal size, and the lowest crystal size (9.3 nm) was observed for HT_Cr.

For MO, the diffraction lines at 30.2, 35.6, 37.2, 43.3, 53.4, 56.9, and 62.5° correspond to magnesioferrite. The diffraction lines at 37.0, 43.0, and 62.4° correspond to periclase (MgO). The diffraction lines are broad with low intensity, which correspond to the low crystallinity with a large proportion of the amorphous phase. The typical diffraction lines for oxides of TM (CuO, CoO, etc.) were not present because such oxides are amorphous or have a good dispersion.[15]

After reduction (aMO; Figure 1), (i) diffraction lines (37.0, 43.0, and 62.4°) point to the presence of MgO and (ii) sharp diffraction lines at 44.7 and 65.1° point to the presence of metallic iron and characteristic diffraction line at 42.2° points to the presence of FeO. Therefore, part of iron oxide was reduced to metallic iron at activation conditions (Section 2.1). The diffraction lines for metallic Ni, Co, Mn, or Cr were not

https://doi.org/10.1021/acsomega.3c00182
ACS Omega 2023, 8, 19374−19384

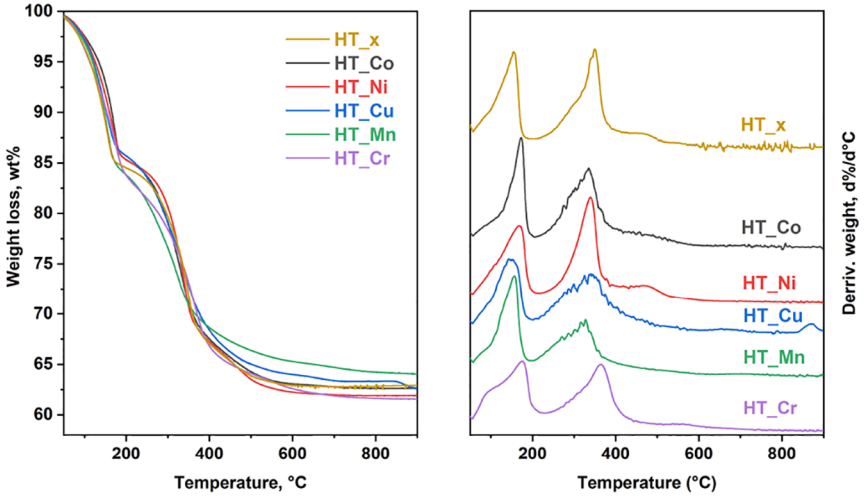

Figure 2. TGA (left) and dTGA (right) curves of Mg-Fe HT.

detected which could be due to (i) well dispersion of such metals in the structure and (ii) only partial reduction of the oxides under activation conditions. In addition, the diffraction lines for CoO, CuO, and NiO (PDF-4) were observed. A partial reduction of TM oxides at activation conditions corresponds to results from H_2-TPR (3.1.3). The diffraction lines for metal Cu (43.2 and 50.6°) were observed, which indicated the reduction of CuO to Cu. For Mn and Cr, the diffraction lines for oxide or metallic form were not observed.

3.1.2. Thermogravimetric Analysis. The thermal stability of HT materials was determined by thermogravimetric analysis (TGA) (Figure 2 and Table 2). Two weight losses on the curves were observed. The first weight loss up to 220 °C was corresponding to water release from the interlayer,.[16] The first weight loss was similar for all HT and ranged from 14.8 to 17.4 wt %. The second weight loss observed up to 528 °C corresponds to decomposition of interlayer and release of carbonate dioxide (from carbonates) and water (from hydroxyls). The second weight loss ranged from 18.2 to 22.2 wt %. The important conclusion is that the presence of TM in a structure has an insignificant effect on the transformation process from HT to MO form. The total weight loss of Mg-Fe HT was between 36 and 39 wt %. On the basis of the TGA result, the temperature for the parent HT calcination was determined at 500 °C.

Table 2. TGA Results for X-Mg-Fe HT

type of TM	1st weight loss, wt %	1st T_{max}, °C	2nd weight loss, wt %	2nd T_{max}, °C
x	15.3	155	21.3	349
Co	14.8	172	21.6	335
Ni	15.0	169	22.2	340
Cu	14.2	147	21.3	341
Mn	15.9	155	18.2	329
Cr	17.4	175	19.1	365

3.1.3. Temperature-Programmed Reduction with H_2. The reduction properties of MO were studied using the H_2-TPR technique. Related reduction profiles are presented in Figure 3 and maxima of observed features in Table 3. Due to the very high reduction potential of magnesium (absolute value), the present contributions are attributed to the reduction of iron and the second TM in the oxide structure. All TMs were reduced in the 35−1000 °C interval. MO_x, a sample without the second TM, shows two dominant contributions corresponding to the reduction of Fe. The second TM (Co, Ni, Cu, Mn, or Cr) causes a shift in the reduction maxima of Fe and the occurrence of further reduction maxima due to the reduction of the second TM. Compared to the previously studied Mg-Al MO,[10] the structure of Mg-Fe MO causes significant changes in the reducibility of the second TM: reductions are less defined and shifted to lower temperatures. The resolution of the contributions of the Fe reduction and the second TM reduction is not straightforward due to overlapping reduction peaks. In the case of Cu, it is possible to observe a

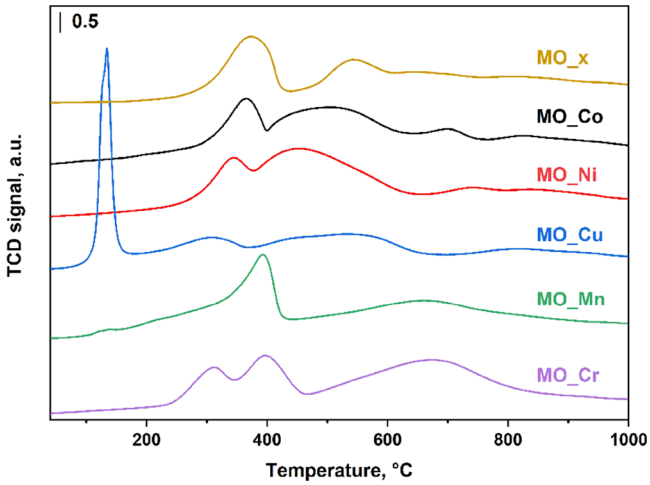

Figure 3. TPR curves of Mg-Fe MO.

Table 3. TPR Maxima and Acid−Base Properties of aMO

type of TM	TPR maxima, °C	CBS on aMO, μmol g^{-1}	CAS on aMO, μmol g^{-1}
x	374; 545; 645	64.9	32.0
Co	366; 506; 698; 825	60.2	23.0
Ni	344; 451; 741	77.4	24.2
Cu	137; 308; 532; 815	66.4	18.7
Mn	393; 659	96.1	33.0
Cr	312; 397; 674	142.7	103.4

https://doi.org/10.1021/acsomega.3c00182
ACS Omega 2023, 8, 19374−19384

separated reduction peak of CuO at maximum 137 °C, which is significantly lower compared to the reduction of bulk CuO (in the range of 200−300 °C[17,18]). Furthermore, the presence of CuO in the mixed Mg-Fe oxide also causes a decrease in the reduction maxima of iron (374−308 °C; 545−532 °C). It is therefore clear that the mutual interaction of CuO and Mg-Fe mixed oxide causes a decrease in the reduction potential of both copper and iron. Although for other catalysts, the reduction contributions are not as well distinguished as in the case of MO_Cu, the same conclusion about the decrease of the reduction potentials of TMs in mixed Mg-Fe oxide can be also drawn, being in accordance with observations presented before.[10,19]

The catalyst activation temperature was set at 450 °C (Section 2.2 Catalyst Testing) to prevent the formation of spinel structures. Spinel structures are generally considered to have lower specific surface area and acido-basicity and therefore less catalytically active in the reactions related to these catalyst features.[20,21] Since some oxides showed lower hydrogen reduction rates at 450 °C, a longer prereduction time of 5 h proceeded to reach the catalyst with Fe and TM in the lowest possible oxidation state (in average). It has to be noted that the catalysts activated at 450 °C may not be completely reduced. On the one hand, the complete reduction of Fe ends at higher temperatures, and on the other hand, the reduction of the second TM (except Cu) also ends at higher temperatures than the activation temperature of 450 °C. At this temperature, the group of catalysts MO_Co, MO_Cu, and MO_Ni shows high reduction rates, and the group MO_Mn and MO_Cr shows low reduction rates. H_2-TPR results correspond to XRD results on aMOs (Section 3.1.1) where diffraction lines of TM oxides were detected. The blurring of the reduction peaks and the presence of reduction traces at higher temperatures are due to the phase inhomogeneity of the samples. At the beginning of the catalytic reaction tests, a certain amount of TM is not present in the metallic state, particularly for the MO_Mn and MO_Cr samples with reductions at higher temperatures.

3.1.4. N_2-Physisorption and Specific Surface Area. The texture of aMO was studied using N_2-physisorption (Figure S1). The isotherms are type IV, revealing the mesoporous structure of all studied aMOs. The hysteresis loops, connected with the capillary condensation phenomena, are type H3, pointing to agglomerates of platelike particles forming slit pores in the interparticle space.[22] The exception is the hysteresis loop of aMO_Cr, which between the types H2 and H3, related to the disordered porous material with a wide distribution of pore shape creating larger free volumes at the point of pore intersection. The different pore shape of aMO_Cr corresponds to a different crystallographic structure, where only diffraction lines for MgO and magnesioferrite were observed, and the diffraction lines were broader with a low intensity associated with the amorphous character. Hysteresis loops of aMO_x and aMO_Co are relatively narrow showing a small contribution of the capillary condensation.

The distribution of pore sizes was calculated using the NLDFT method (Figure S1). For all aMOs, the distribution of pore sizes ranged from 3 to 60 nm. This relative wide distribution of mesopores was observed also by other authors for MO of similar composition and synthesis.[23,24] Only a small contribution of micropores (≤2 nm) was detected for all aMO. The maximum at the distribution curves points to the abundance of pores of 8−10 nm. The exception is pure aMO_x with dominant pores at 5 nm, which has also the lowest total pore volume of 0.117 $cm^3\ g^{-1}$ (Table 4). Conversely, the pore volume of aMO_Cr is the highest reaching 0.360 $cm^3\ g^{-1}$.

Table 4. Specific Surface Area for Mg-Fe MO and aMO and Pore Volume of aMO

	S_{BET}, $m^2\ g^{-1}$		V_{meso}, $cm^3 g^{-1}$	V_{total}, $cm^3 g^{-1}$
type of TM	MO	aMO	aMO	aMO
x	101	42	0.099	0.117
Co	95	57	0.165	0.200
Ni	101	58	0.220	0.278
Cu	102	59	0.196	0.252
Mn	99	67	0.194	0.239
Cr	143	112	0.346	0.360

The specific surface area (S_{BET}) was calculated by the BET equation for both MO and aMO forms (Table 4). The activation (reduction) corresponds to the structure and texture changes, which caused the significant reduction of S_{BET} after activation. The S_{BET} was determined in the range of 95−143 $m^2\ g^{-1}$ for MO and in the range of 42−112 $m^2\ g^{-1}$ for aMO. The relative decrease of the S_{BET} ranged from 22 to 58%. The highest surface reduction was determined for pure MO_x and the lowest for MO_Cr. The observed S_{BET} values are rather lower compared to MO with similar composition published earlier (220 $m^2\ g^{-1}$), which is probably due to the different calcination temperatures affecting the structure of the individual catalysts used in the studies being compared.[23] The presence of magnesioferrite (41.7 $m^2\ g^{-1}$)[25,26] can lead to the decrease of the specific surface area.

3.1.5. TPD. The amount and distribution of Lewis basic and acidic sites on the surface of Mg-Fe aMO were studied using CO_2-TPD and NH_3 techniques, respectively. The measured CO_2 desorption curves in the range of 35−500 °C are presented in Figure 4, and the NH_3 desorption curves in the range of 70−500 °C are presented in Figure 5. The concentration of basic and acidic sites (Table 3) was obtained by integrating the area under the TPD curve. The TPD curve

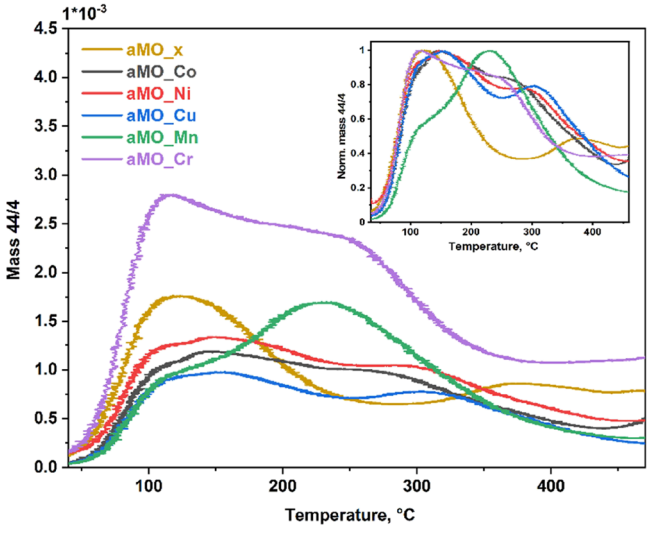

Figure 4. CO_2-TPD curves and normalized 0−1 curves on Mg-Fe aMO.

https://doi.org/10.1021/acsomega.3c00182
ACS Omega 2023, 8, 19374−19384

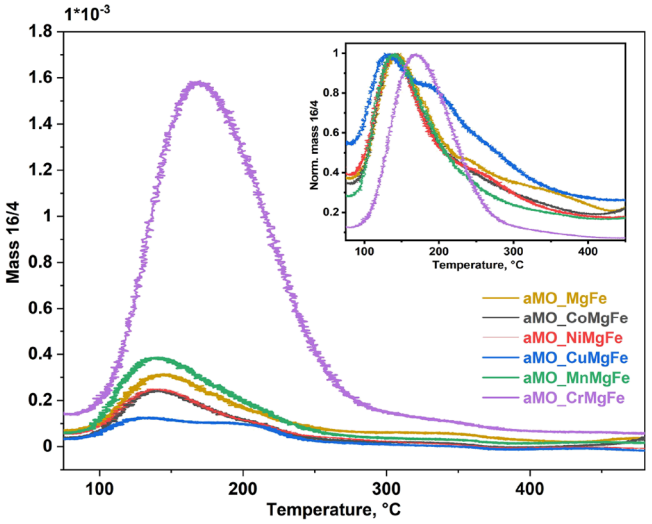

Figure 5. NH_3-TPD curves and normalized 0−1 curves on Mg-Fe aMO.

of aMO without gas saturation (preadsorption) was used as a baseline.

The composition of the aMO affects the concentration and distribution of basic sites. The concentration of basic sites on aMO increases in the order Co < x < Cu < Ni < Mn < Cr. The difference in the concentration is due to (i) the presence of TM (oxides) in the Mg-Fe MO structure and (ii) the varying amounts of oxide surface defects produced in the process of the activation of catalyst (reduction of Fe and TM under H_2 pressure) (Section 3.1.3). In this line, the catalysts aMO_Cr and aMO_Mn bear higher basicity.

Compared to the previously studied Mg-Al aMO,[10] the present Mg-Fe aMO exhibits significantly lower basicity. This observation corresponds to previously published results on bimetallic Mg-Al and Mg-Fe MO with comparable X^{+II}/Y^{+III} ratio.[27,28] The CO_2-TPD curves show several different overlapping contributions corresponding to the basic sites of different strengths.[29,30] Weakly basic OH^- groups are observed at the lowest temperatures, medium strong Me^{n+}-O^{2-} pairs at medium temperatures, and unsaturated O^{2-} sites at the highest temperatures.[31] The differences in the populations of the individual sites (their relative amounts) are seen on the normalized curves (Figure 4). The aMO_x catalyst shows the lowest population of medium strong Me^{n+}-O^{2-} pairs, whereas aMO_Mn shows the highest population of such pairs. For other catalysts, the differences in the distribution of basic sites are not pronounced.

In addition, the composition of the aMO significantly affects the amount of acid sites. The concentration of acid sites on aMO increases in the order Cu < Co < Ni < x < Mn < Cr. The differences among concentrations on the aMO_Cu, Co, and Ni are not much pronounced. Catalyst aMO_Cr significantly reveals the highest concentration of acid sites and catalyst aMO_Cu the lowest. The highest concentration of Lewis basic and acidic sites on aMO_Cr and aMO_Mn would be related to the lowest reducibility (Section 3.1.3) and the presence of a large amount of Cr and Mn oxides on the catalyst surface even after activation in H_2 at 450 °C.

Compared to previously studied series of Mg-Al aMO catalysts, present Mg-Fe aMO is less acidic (several times). In our earlier studies on Mg-Al and Mg-Fe MO (calcined HT), we showed that Mg-Fe has generally lower concentration of surface acid Me^{3+} sites.[30] The NH_3-TPD curves peaked at around 120−150 °C. Peaks show asymmetry on the higher temperature side, corresponding to a heterogeneity of acidic Me^{n+} sites. Catalysts of aMO_x, Co, Ni, and Mn exhibit similar distribution of acid sites, and catalysts aMO_Cr and aMO_Cu exhibit a higher population of sites with higher acidity.

3.2. Reaction. The products of ethanol transformation, including reaction mechanisms, were described in previous publication in detail (the reduced Mg-Al MOs with different

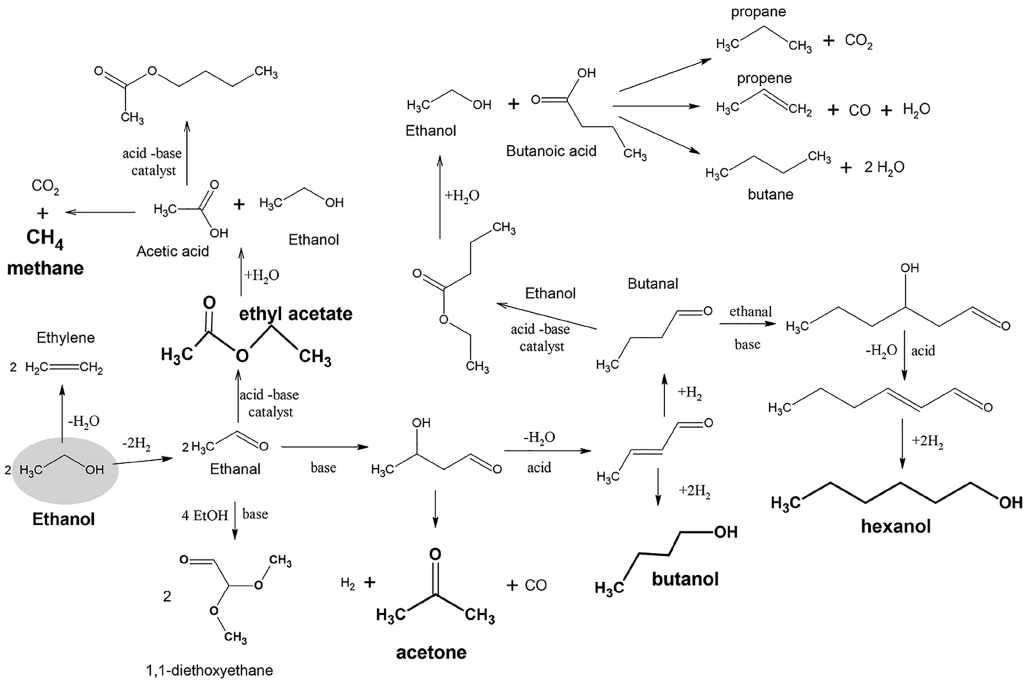

Figure 6. Proposed scheme of transformation of ethanol by Mg-Fe catalysts.

https://doi.org/10.1021/acsomega.3c00182
ACS Omega 2023, 8, 19374−19384

TMs were used[10]). Ethanol can be either (i) dehydrated to ethylene[2] or (ii) dehydrogenated/partially oxidized to ethanal.[32] The resulting ethanal (aldehyde with αH) can react by (i) aldol-condensation to crotonaldehyde, which is subsequently hydrogenated to butanol or (ii) Tishchenko reaction (two aldehydes) to esters (ethyl acetate). Both reactions are catalyzed by the acid−base catalysts,[8,33] nevertheless, the Tishchenko reaction relates to the catalysts with higher Lewis acidity and lower basicity.[34] The intermediate of aldol-condensation is acetaldol, which can react to form acetone, carbon monoxide, and hydrogen. The crotonaldehyde can be hydrogenated fully to butanol or partially to butanal, followed by the formation of hexanol and 2-ethylbutan-1-ol (aldol-condensation) or butyl butanoate (Tishchenko reaction). Moreover, ethers can be formed by the reaction of aldehydes with alcohols (ethanol or formed butanol). The esters (formed by Tishchenko reaction) hydrolyzed in the presence of acid catalysts to carboxylic of acids, which can undergo the (trans)esterification with other alcohols to esters in the presence of acid−base catalysts.[35] The decarboxylation, decarbonylation, and hydrodeoxygenation could be carried out at higher temperatures on metallic centers of the catalysts leading to the formation of hydrocarbon gases, CO_2, CO, and water.[36,37] The type of catalyst and the reaction condition play an important role in controlling the reaction to form the desired product(s). Nevertheless, comparison of catalytic results and activities of individual used catalysts among publications is not straightforward, mainly due to different reaction conditions such as the type of reactor (bath or flow with different weight hour space velocity), temperature (60−500 °C), pressure (0.1−10 MPa), and reaction time (2−150 hod)[38] used. Particularly for the catalysts based on LDH-based mixed oxides, different types and contents of metals and ways of syntheses are used.[39] The observed ethanol conversion is in the wide range from 0 to 90%, and the composition of reaction mixture varies. Therefore, catalytic tests at the same conditions are necessary to show the effect of catalyst composition.

In this contribution, a number of liquid and gas products from the ethanol conversion were analyzed, and the scheme of reaction mechanism was significantly extended (Figure 6).

The conversion of ethanol was determined at 300 °C for all Mg-Fe aMOs (Figure 7). Specific trends for individual TMs observed here are in line with our results presented before for Mg-Al aMO measured at the same reactor and catalytic conditions.[10] The catalyst Mg-Fe without a second TM achieves a twice higher ethanol conversion than Mg-Al. Therefore, iron present in Mg-Fe aMO exhibits certain redox properties and dehydrogenates ethanol at the given reaction conditions. The significant differences of the composition between Mg-Fe and Mg-Al_aMO series cause the different formed products, which suggest different reaction pathways. For the Mg-Al aMO series, the main products of the reaction are Guerbet alcohols,[10] while for Mg-Fe aMO series, the presence of esters as products of the Tishchenko reaction is observed. The substitution of Al for Fe led to a drop of the concentration of acid−base active sites (Section 3.1.5).[10] The decrease in the population of aldolization products on Mg-Fe compared to Mg-Al catalysts is due to a lower concentration of basic sites and a significantly lower concentration of acidic centers on the surface of Mg-Fe catalysts.

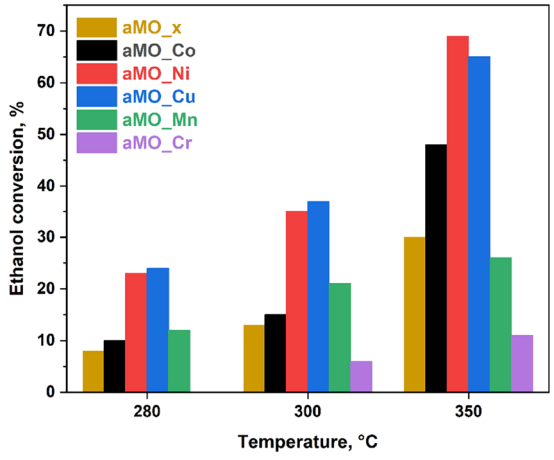

Figure 7. Values of ethanol conversion at temperatures 280, 300, and 350 °C for Mg-Fe catalysts.

The ethanol conversion increased with the reaction temperature (280−350 °C) for all tested samples (Figure 7). The example of ethanol conversion over time for aMO_x is shown in Figure S2. The catalysts aMO_Ni and aMO_Cu were observed to be the most active in the whole range 280−350 °C. The ethanol conversion associated with the dehydrogenation activity was very similar for both aMO_Ni and aMO_Cu. While aMO_x, aMO_Ni, aMO_Cu, and aMO_Co catalysts were related to the strong activation with the temperature, aMo-Mn and aMo-Cr catalysts showed relatively lower dependence of ethanol conversion on the temperature. In particular, the highest conversion of ethanol (65−70%) at 350 °C was reached for aMO-Ni and aMO-Cu catalysts.

The addition of a second TM to Mg-Fe aMO clearly modifies the value of ethanol conversion. Compared to aMO_x, metals Co, Ni, Cu, and Mn increased the catalyst activity. Marked increase of conversion was detected for Cu and Ni (aMO_x X_{Eth} = 13%; aMO_Cu X_{Eth} = 37%; aMO_Ni X_{Eth} = 35% at temperature 300 °C). aMO_Co, aMO_Ni, and aMO_Cu catalysts were related to the similar acido-basic (Section 3.1.4) and specific surface areas (Section 3.1.5) but the different ethanol conversions. The presence of Cr in Mg-Fe was related to a low catalyst activity (aMO_Cr X_{Eth} < 1% at 280 °C). Despite the relatively higher (i) concentration of acid−base sites (Section 3.1.5), (ii) acidity of sites (Section 3.1.5), and (iii) specific surface area and pore volume (Section 3.1.4), aMO_Cr catalyst has scarce activity in ethanol conversion at 280 °C. It can be assumed that differences in activity across studied Mg-Fe aMO catalysts are given by the redox properties (Section 3.1.2) and the ability of a second TM to dehydrogenate ethanol at the given reaction conditions. Chromium has not sufficient redox activity, which is related to the highest temperature needed for the reduction of Cr on Mg-Fe (3.1.3). At 450 °C, which is the activation temperature of the catalyst, the majority of chromium remained unreduced, and within the catalytic experiment in the interval 280−350 °C, the redox cycle for the reduction−oxidation of Cr did not apply. The aMO_Cr catalyst shows ethanol conversions only at higher reaction temperatures, which are still relatively low compared to the other catalysts. The highest active aMO_Ni and aMO_Cu catalysts show very similar ethanol conversions across the temperature range, although their reducibility is different (Section 3.1.3). Catalytic activity, the conversion of ethanol, would depend not only on the reducibility of the metal but also on the dispersion of active metal particles

https://doi.org/10.1021/acsomega.3c00182
ACS Omega 2023, 8, 19374−19384

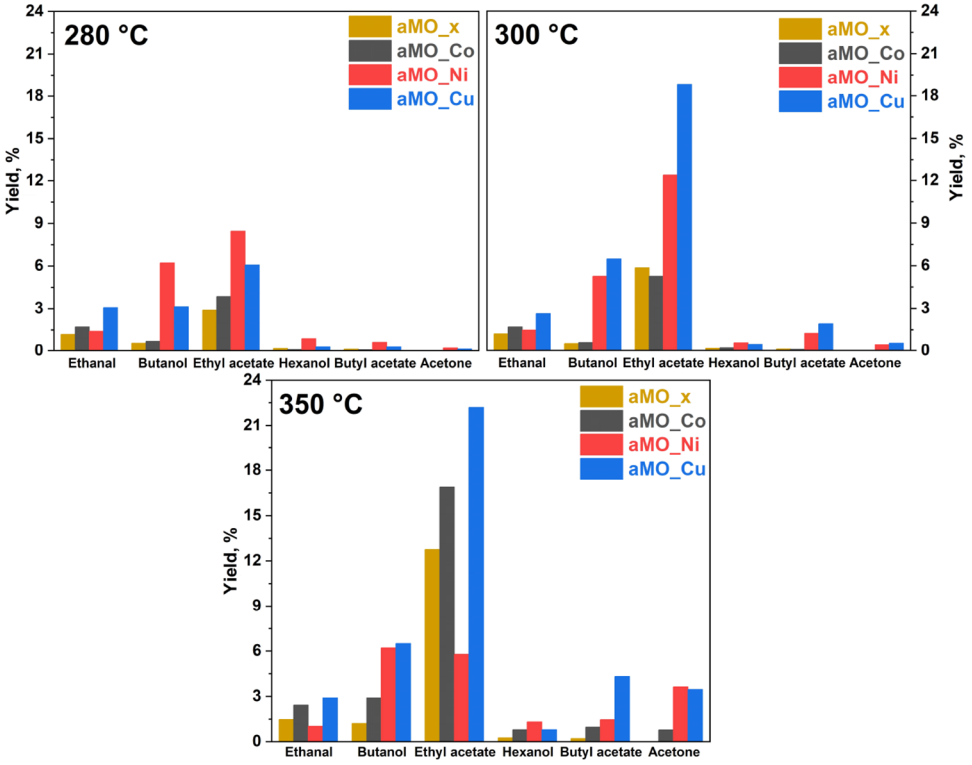

Figure 8. Yields of products at temperatures 280, 300s and 350 °C for selected Mg-Fe catalysts.

(particle sizes) on the surface of the mixed oxide.[40,41] This topic is beyond the scope of this paper and would be the subject of further in-depth study of these MO catalysts. Additionally, the catalytic results on Mg-Fe series lead to conclusions that acid−base sites do not significantly contribute to the ethanol conversion even at 350 °C. According to the previous study, acid−base sites apply in ethanol dehydrogenation only at higher temperatures.[9]

The yield of detected product liquids at RT (reaction temperature) is discussed for the three most active catalysts at 350 °C, aMO_Co, aMO_Ni, and aMO_Cu, and compared to aMO_x (without a second TM) (Figure 8). For less active aMO_Mn and aMO_Cr catalysts, the yield is shown in Figure S3. However, the yield values for aMO_Mn and aMO_Cr catalysts are burdened with a relatively high error due to the low conversion of ethanol achieved. The composition of a catalyst is in strong relation to the distribution of products in a complex reaction scheme (Figure 6). In the reaction mixture, ethyl acetate was observed as the main product of the ethanol conversion. Butanol and ethanal were also detected in relatively large amounts. Additionally, hexanol, butyl acetate, and acetone were detected. The product redistribution in the temperature interval 280−350 °C was observed. Butyl acetate and acetone were relatively more abundant at higher temperatures. Butyl acetate yield increased with increasing temperature markedly in the case of aMO_Cu.

At the temperature of 280 °C, the yield of main products ethyl acetate and butanol was the highest for the aMO_Ni catalyst. At higher temperatures, 300 and 350 °C, ethyl acetate and butanol were dominating for the aMO_Cu catalyst. aMO_Cu and aMO_Co catalysts were related to the enhanced production of such products at higher temperatures. For aMO_Ni, the reduced yield of ethyl acetate and butanol going from 300 to 350 °C was detected. This is due to the support of refining processes, being related to cleavage of C−C bonds, leading to a higher presence of gases on aMO-Ni, as demonstrated in Figure S4, on the population of the products in the gas phase at RT. The gas production increased relatively with the temperature. Among gases, hydrogen had the highest proportion, which indicates the support of the dehydrogenation step and/or suppressed hydrogenation step in subsequent reactions. This is completely in line with the yield of butanol and hexanol, which were formed by the hydrogenation. The presence of CH_4 and CO_2, which were formed by the decarboxylation, is crucial. The highest proportion of CH_4 and CO_2 was observed in the case of the aMO_Ni, which correlates with a lower acetate yield. Therefore, it is argued that aMO_Ni promoted the hydrolysis of acetate to carboxylic acids, which were subject to decarboxylation.

The higher temperature promotes the formation of higher Guerbet alcohols, among which hexanol has also been detected. It was the yield of hexanol that increased with temperature. The evolution of Guerbet alcohols with temperature was observed despite the yield of ethanal not obviously affected by the temperature. Acetone is a byproduct of the Guerbet reaction. An increase in acetone yield was observed with increasing temperature from 300 to 350 °C. The highest yield was detected for aMO_Cu and aMO_Ni.

At 350 °C, ethylene, which was formed by the dehydration of ethanol, was observed in the case of aMO_x and aMO_Co. Butane and propane were also observed for aMO_Co. This confirms that the hydrodeoxygenation, decarboxylation, and decarbonylation of butanoic acid, which results from the decomposition of butanoate, took place.

The catalyst stability was also tested for all aMOs. The starting reaction temperature of 300 °C was reset after 96 h of running the reaction, and other reaction parameters were kept constant. The test was carried out for the next 32 h. Only

https://doi.org/10.1021/acsomega.3c00182
ACS Omega 2023, 8, 19374−19384

slightly decreased ethanol conversion was observed, which suggests a stable structure of all aMO catalysts. The decreased conversion could be caused by coking at higher temperature (350 °C), which was related to a change of catalyst color to a darker one after reaction. The real amount of coke could not be determined due to the problematic separation of the catalyst from the mixture with silicon carbide (inert for dilution to keep constant contact time). The large amount of strongly interacting reaction components also could not be selectively removed in the temperature range of the reaction or even with the use of solvents. Therefore, characterizations after the reaction are not possible. For the stability test, moreover, the metal content potentially leached from the catalyst in liquid products was measured. For all tested aMO catalysts, no metals were detected in the product mixture (the detection limit was 1 mg/kg). Ethylene production was detected to be very low (Figure S4), so the probability of polyethylene formation and associated deactivation by polymerization was low. Despite small coking, the catalysts are stable in reaction during the 128 h, which is convenient for the possible future applications (scale-up). The products of reaction are possible to be separated by the rectification.

4. CONCLUSIONS

Ethanol was converted to several (petro)chemicals in a flow reactor using the reduced mixed oxides Mg-Fe with various TMs (Cu, Cr, Co, Mn, and Ni) with a constant metal ratio and reaction conditions. The decrease in the population of aldolization products on Mg-Fe compared to Mg-Al catalysts was due to a lower concentration of basic sites and a significantly lower concentration of acidic centers on the surface of Mg-Fe catalysts. In the Mg-Fe series, the highest conversion of ethanol was determined for aMO_Ni and the lowest for aMO_Cr. The differences in activity across studied Mg-Fe aMO catalysts were given by the redox properties and the ability of a second TM to dehydrogenate ethanol at the given reaction conditions. The chromium had no sufficient redox activity. The significant yield of ethyl acetate was observed for Ni and Cu in the whole temperature interval 280−350 °C. Copper supports formation of acetates even at higher temperatures. For aMO-Ni catalysts, the gasification of products was confirmed by the presence of gases, especially methane. Based on a number of products detected in the liquid phase and also gas phase at RT, the pathways of ethanol conversion were extended. The long-term catalyst stability was verified by negligible leaching of metals, but simultaneous carbonization proceeded.

ASSOCIATED CONTENT

Supporting Information

The Supporting Information is available free of charge at https://pubs.acs.org/doi/10.1021/acsomega.3c00182.

Real molar ratios of metals in MOs used in this study; graphs of nitrogen isotherms and pore size distribution of Mg-Fe aMO used in this study; dependence of ethanol conversion on time for the Mg-Fe catalyst without a second TM; yields of reaction products at temperatures 280, 300, and 350 °C for Cr and Mn Mg-Fe catalysts; and amounts of gaseous products at temperatures 280, 300, and 350 °C for selected Mg-Fe catalysts (PDF)

AUTHOR INFORMATION

Corresponding Author

Jaroslav Kocík − *ORLEN UniCRE, 400 01 Ústí nad Labem, Czech Republic;* orcid.org/0000-0001-5004-5889; Email: jaroslav.kocik@orlenunicre.cz

Authors

Jáchym Mück − *Department of Physical Chemistry, Faculty of Chemical Technology, University of Pardubice, 532 10 Pardubice, Czech Republic;* orcid.org/0000-0003-3424-7688

Karel Frolich − *Department of Physical Chemistry, Faculty of Chemical Technology, University of Pardubice, 532 10 Pardubice, Czech Republic;* orcid.org/0000-0002-9616-942X

Josef Šimek − *ORLEN UniCRE, 400 01 Ústí nad Labem, Czech Republic*

Martina Michálková − *ORLEN UniCRE, 400 01 Ústí nad Labem, Czech Republic*

Martin Hájek − *Department of Physical Chemistry, Faculty of Chemical Technology, University of Pardubice, 532 10 Pardubice, Czech Republic*

Complete contact information is available at: https://pubs.acs.org/10.1021/acsomega.3c00182

Notes

The authors declare no competing financial interest.

ACKNOWLEDGMENTS

This work was supported by the University of Pardubice, Czech Republic, project SGS_2023_008. The result was achieved using the infrastructure included in the project Efficient Use of Energy Resources Using Catalytic Processes (LM2018119) which has been financially supported by MEYS within the targeted support of large infrastructures.

NOMENCLATURE

HT	hydrotalcite-like compounds
MO	mixed oxides
aMO	reduced mixed oxides
BET	Brunauer, Emmett and Teller theory
ICP-OES	inductively coupled plasma - optical emission spectrometry
NLDFT	nonlocal density functional theory
TGA	thermogravimetric analysis
TPD	temperature-programmed desorption
TPR	temperature-programmed reduction
XRD	X-ray diffraction
TM	second transition metal (Co, Ni, Cu, Mn or Cr)
RT	reaction temperature
S_{BET}	specific surface area, $m^2\ g^{-1}$
a, c	hydrotalcite lattice parameters, nm
CAS	concentration of acid sites, $\mu mol\ g^{-1}$
CBS	concentration of basic sites, $\mu mol\ g^{-1}$
D	crystallite size of hydrotalcites, nm
S_P	product selectivity, %
X_E	conversion of ethanol, %

REFERENCES

(1) Pampararo, G.; Garbarino, G.; Comite, A.; Busca, G.; Riani, P. Acetaldehyde production by ethanol dehydrogenation over Cu-ZnAl2O4: Effect of catalyst synthetic strategies on performances. *Chem. Eng. Sci.* **2022**, *261*, No. 117937.

(2) Srinivasan, P. D.; Khivantsev, K.; Tengco, J. M. M.; Zhu, H.; Bravo-Suárez, J. J. Enhanced ethanol dehydration on γ-Al2O3 supported cobalt catalyst. *J. Catal.* **2019**, *373*, 276−296.
(3) Zhukova, A. I.; Chuklina, S. G.; Maslenkova, S. A. Study of Cu modified Zr and Al mixed oxides in ethanol conversion: The structure-catalytic activity relationship. *Catal. Today* **2021**, *379*, 159−165.
(4) León, M.; Díaz, E.; Ordóñez, S. Ethanol catalytic condensation over Mg−Al mixed oxides derived from hydrotalcites. *Catal. Today* **2011**, *164*, 436−442.
(5) Inui, K.; Kurabayashi, T.; Sato, S. Direct Synthesis of Ethyl Acetate from Ethanol Carried Out under Pressure. *J. Catal.* **2002**, *212*, 207−215.
(6) Inui, K.; Kurabayashi, T.; Sato, S. Direct synthesis of ethyl acetate from ethanol over Cu-Zn-Zr-Al-O catalyst. *Appl. Catal., A* **2002**, *237*, 53−61.
(7) Adesina, A. Y.; Obot, I. B.; Sorour, A. A.; Mtongana, S.; Mamilla, S. B.; Almathami, A. A. Corrosion challenges and prevention in Ethyl Acetate (EA) production and related processes − An overview. *Eng. Fail. Anal.* **2021**, *127*, No. 105511.
(8) Brasil, H.; Bittencourt, A. F. B.; Yokoo, K. C. E. S.; Mendes, P. C. D.; Verga, L. G.; Andriani, K. F.; Landers, R.; Da Silva, J. L. F.; Valença, G. P. Synthesis modification of hydroxyapatite surface for ethanol conversion: The role of the acidic/basic sites ratio. *J. Catal.* **2021**, *404*, 802.
(9) Tsuchida, T.; Kubo, J.; Yoshioka, T.; Sakuma, S.; Takeguchi, T.; Ueda, W. Reaction of ethanol over hydroxyapatite affected by Ca/P ratio of catalyst. *J. Catal.* **2008**, *259*, 183−189.
(10) Mück, J.; Kocík, J.; Hájek, M.; Tišler, Z.; Frolich, K.; Kaňpárek, A. Transition metals promoting Mg-Al mixed oxides for conversion of ethanol to butanol and other valuable products: Reaction pathways. *Appl. Catal., A* **2021**, *626*, No. 118380.
(11) Shannon, R. D. Revised effective ionic radii and systematic studies of interatomic distances in halides and chalcogenides. *Acta Crystallogr. A* **1976**, *32*, 751−767.
(12) Rozov, K. B.; Berner, U.; Kulik, D. A.; Diamond, L. W. Solubility and Thermodynamic Properties of Carbonate-Bearing Hydrotalcite-Pyroaurite Solid Solutions with A 3:1 Mg/(Al+Fe) Mole Ratio. *Clays Clay Miner.* **2011**, *59*, 215−232.
(13) Gonçalves, R. G. L.; Mendes, H. M.; Bastos, S. L.; D'Agostino, L. C.; Tronto, J.; Pulcinelli, S. H.; Santilli, C. V.; Neto, J. L. Fenton-like degradation of methylene blue using Mg/Fe and MnMg/Fe layered double hydroxides as reusable catalysts. *Appl. Clay Sci.* **2020**, *187*, No. 105477.
(14) Bernard, E.; Zucha, W. J.; Lothenbach, B.; Mäder, U. Stability of hydrotalcite (Mg-Al layered double hydroxide) in presence of different anions. *Cem. Concr. Res.* **2022**, *152*, No. 106674.
(15) Carriazo, D.; del Arco, M.; Martín, C.; Rives, V. A comparative study between chloride and calcined carbonate hydrotalcites as adsorbents for Cr(VI). *Appl. Clay Sci.* **2007**, *37*, 231−239.
(16) Yang, W.; Kim, Y.; Liu, P.; Sahimi, M.; Tsotsis, T. A study by in situ techniques of the thermal evolution of the structure of a Mg−Al−CO3 layered double hydroxide. *Chem. Eng. Sci.* **2002**, *57*, 2945−2953.
(17) Wang, Z.; Niu, Z.; Hao, Q.; Ban, L.; Li, H.; Zhao, Y.; Jiang, Z. Enhancing the Ethynylation Performance of CuO-Bi2O3 Nano-catalysts by Tuning Cu-Bi Interactions and Phase Structures. *Catalysts* **2019**, *9*, 35.
(18) Scotti, N.; Marelli, M.; Psaro, R.; Ravasio, N. Unravelling the Properties of Supported Copper Oxide: Can the Particle Size Induce Acidic Behavior? *Dalton Trans.* **2013**, *42*, 1319.
(19) Melo, F.; Morlanés, N. Study of the composition of ternary mixed oxides: Use of these materials on a hydrogen production process. *Catal. Today* **2008**, *133-135*, 374−382.
(20) Qin, F.-J.; Liu, Y.-J.; Qing, S.-J.; Hou, X.-N.; Gao, Z.-X. Cu-Al spinel as a sustained release catalyst for H2 production from methanol steam reforming: Effects of different copper sources. *J. Fuel Chem. Technol.* **2017**, *45*, 1481−1488.
(21) Hájek, M.; Tomášová, A.; Kocík, J.; Podzemná, V. Statistical evaluation of the mutual relations of properties of Mg/Fe hydrotalcites and mixed oxides as transesterification catalysts. *Appl. Clay Sci.* **2018**, *154*, 28−35.
(22) Sing, K. Reporting Physisorption Data for Gas/Solid Systems with Special Reference to the Determination of Surface Area and Porosity. *Pure Appl. Chem.* **1982**, *54*, 2201−2218.
(23) Guerrero-Urbaneja, P.; García-Sancho, C.; Moreno-Tost, R.; Mérida-Robles, J.; Santamaría-González, J.; Jiménez-López, A.; Maireles-Torres, P. Glycerol valorization by etherification to polyglycerols by using metal oxides derived from MgFe hydrotalcites. *Appl. Catal., A* **2014**, *470*, 199−207.
(24) Hanif, A.; Sun, M.; Wang, T.; Shang, S.; Tsang, D. C. W.; Shang, J. Ambient NO2 adsorption removal by Mg−Al layered double hydroxides and derived mixed metal oxides. *J. Cleaner Prod.* **2021**, *313*, No. 127956.
(25) Zhou, L.; Liu, J.; Lu, A.; Shen, J.; Xu, J.; Jiang, H. Controllable synthesis of cubic magnetic MgFe2O4 derived from MgFe-LDHs for efficient removal of methyl orange. *Chem. Eng. J.* **2022**, *428*, No. 131174.
(26) Obata, K.; Doi, A.; Nishibori, M.; Shimanoe, K.; Suzuki, T.; Matsushima, S. Morphology, microstructure, and surface area of La-added $MgFe_2O_4$ powder. *J. Ceram. Soc. Jpn.* **2018**, *126*, 402−407.
(27) Di Cosimo, J. I.; Diez, V. K.; Xu, M.; Iglesia, E.; Apesteguia, C. R. Structure and Surface and Catalytic Properties of Mg-Al Basic Oxides. *J. Catal.* **1998**, *178*, 499−510.
(28) Smoláková, L.; Frolich, K.; Kocík, J.; Kikhtyanin, O.; Čapek, L. Surface Properties of Hydrotalcite-Based Zn(Mg)Al Oxides and Their Catalytic Activity in Aldol Condensation of Furfural with Acetone. *Ind. Eng. Chem. Res.* **2017**, *56*, 4638−4648.
(29) Kikhtyanin, O.; Čapek, L.; Smoláková, L.; Tišler, Z.; Kadlec, D.; Lhotka, M.; Diblíková, P.; Kubička, D. Influence of Mg−Al Mixed Oxide Compositions on Their Properties and Performance in Aldol Condensation. *Ind. Eng. Chem. Res.* **2017**, *56*, 13411−13422.
(30) Kocík, J.; Frolich, K.; Perková, I.; Horáček, J. Pyroaurite-based Mg-Fe mixed oxides and their activity in aldol condensation of furfural with acetone: effect of oxide composition. *J. Chem. Technol. Biotechnol.* **2019**, *94*, 435−445.
(31) Debecker, D. P.; Gaigneaux, E. M.; Busca, G. Exploring, Tuning, and Exploiting the Basicity of Hydrotalcites for Applications in Heterogeneous Catalysis. *Chem. − Eur. J.* **2009**, *15*, 3920−3935.
(32) Čičmanec, P.; Ganjkhanlou, Y.; Kotera, J.; Hidalgo Herrador, J. M.; Tišler, Z.; Bulánek, R. The effect of vanadium content and speciation on the activity of VO x /ZrO 2 catalysts in the conversion of ethanol to acetaldehyde. *Appl. Catal., A* **2018**, *564*, 208.
(33) Preedavijitkul, S.; Autthanit, C.; Praserthdam, P.; Jongsomjit, B. Role of Cr on Cu-Cr catalyst via direct ethanol dehydrogenation to ethyl acetate. *J. Environ. Chem. Eng.* **2022**, *10*, No. 107542.
(34) Seki, T.; Nakajo, T.; Onaka, M. The Tishchenko Reaction: A Classic and Practical Tool for Ester Synthesis. *Chem. Lett.* **2006**, *35*, 824−829.
(35) Mowla, O.; Kennedy, E.; Stockenhuber, M. In-situ FTIR study on the mechanism of both steps of zeolite-catalysed hydro-esterification reaction in the context of biodiesel manufacturing. *Fuel* **2018**, *232*, 12−26.
(36) Joshi, N.; Lawal, A. Hydrodeoxygenation of acetic acid in a microreactor. *Chem. Eng. Sci.* **2012**, *84*, 761−771.
(37) Crawford, J. M.; Jasinski, J. B.; Carreon, M. A. Towards continuous deoxygenation of acetic acid catalyzed by recyclable mono/bi/trimetallic zeolite catalysts. *J. Catal.* **2021**, *401*, 137−148.
(38) Wu, X.; Fang, G.; Tong, Y.; Jiang, D.; Liang, Z.; Leng, W.; Liu, L.; Tu, P.; Wang, H.; Ni, J.; et al. Catalytic Upgrading of Ethanol to n-Butanol: Progress in Catalyst Development. *ChemSusChem* **2018**, *11*, 71−85.
(39) Marcu, I.-C.; Tanchoux, N.; Fajula, F.; Tichit, D. Catalytic Conversion of Ethanol into Butanol over M−Mg−Al Mixed Oxide Catalysts (M = Pd, Ag, Mn, Fe, Cu, Sm, Yb) Obtained from LDH Precursors. *Catal. Lett.* **2013**, *143*, 23−30.
(40) Sun, Z.; Couto Vasconcelos, A.; Bottari, G.; Stuart, M. C. A.; Bonura, G.; Cannilla, C.; Frusteri, F.; Barta, K. Efficient Catalytic Conversion of Ethanol to 1-Butanol via the Guerbet Reaction over

https://doi.org/10.1021/acsomega.3c00182
ACS Omega 2023, 8, 19374−19384

Copper- and Nickel-Doped Porous. *ACS Sustainable Chem. Eng.* **2017**, *5*, 1738−1746.
(41) Conesa, J. M.; Morales, M. V.; López-Olmos, C.; Rodríguez-Ramos, I.; Guerrero-Ruiz, A. Comparative study of Cu, Ag and Ag-Cu catalysts over graphite in the ethanol dehydrogenation reaction: Catalytic activity, deactivation and regeneration. *Appl. Catal., A* **2019**, *576*, 54−64.

https://doi.org/10.1021/acsomega.3c00182
ACS Omega 2023, 8, 19374−19384